

Slow light-enhanced optical imaging of microfiber radius variations with sub-Ångström precision

Michael Scheucher,^{1,*} Khaled Kassem,^{1,*} Arno Rauschenbeutel,^{1,2} Philipp Schneeweiss,¹ and Jürgen Volz^{1,†}

¹*TU Wien, Atominstitut, Stadionallee 2, 1020 Vienna, Austria*

²*Department of Physics, Humboldt-Universität zu Berlin, 10099 Berlin, Germany*

(Dated: June 16, 2022)

Optical fibers play a key role in many different fields of science and technology. For many of these applications it is of outmost importance to precisely know and control their radius. In this manuscript, we demonstrate a novel technique to determine the local radius variation of a 30 micrometer diameter silica fiber with sub-Ångström precision over more than half a millimeter in a single shot, by imaging the mode structure of the fiber's whispering gallery modes (WGMs). We show that in these WGMs the speed of light propagating along the fiber axis is strongly reduced, which enables us to determine the fiber radius with significantly enhanced precision, far beyond the diffraction limit. By exciting several different axial modes at different probing fiber positions, we verify the precision and reproducibility of our method and demonstrate that we can achieve a precision better than 0.3 Å. The demonstrated method can be generalized to other experimental situations where slow light occurs and, thus, has a large range of potential applications in the realms of precision metrology and optical sensing.

I. INTRODUCTION

The resolution of optical far-field imaging systems is typically limited by diffraction. As a consequence, it is not possible to discern details that are closer together than half of the wavelength of the imaging light. Even for high-end objectives with $NA \approx 1$, this limits the resolution, when using visible light, to a few hundred nanometer. At the same time, the position of point-like scatterers or emitters can be determined with almost arbitrary precision by fitting the point-spread function to the image [1]. This technique is extensively used in super-resolution microscopy [2] or quantum technology [3] and, for optical light fields, yields a position accuracy down to a few nanometers. Nevertheless, the observation of sub-wavelength structures and size variations of macro- and microscopic objects is still an outstanding challenge. For example, the fabrication of optical fibers, which are the central component in modern telecommunication and emerging technologies, does not allow a direct control of the local radius. Since the propagation constant and the group-velocity dispersion of the fiber-guided light strongly depends on the radius, its precise knowledge is important for many applications.

A standard method to determine the size of objects with a resolution at the nanometer scale is scanning electron microscopy (SEM). But, this is experimentally complex and subject to different problems such as the charging of dielectric structures which significantly reduces the measurement accuracy. Several methods that use fiber-guided light to determine the fiber radius have been demonstrated [4–9]. However, non of these methods provide good axial and nanometer-scale radial resolution at

the same time. Scanning methods using external probes, via e.g., a second fiber, allow good axial and radial resolution [10, 11], but are inherently subject to a very low measurement bandwidth, as the probe fiber has to be mechanically moved. Furthermore, the direct contact between the two fibers might alter the outcome of the measurement and potentially damages the sample when scanning the position along the fiber. Other approaches, including measuring the force–elongation curve [12] or direct optical imaging methods [13, 14], do not achieve sufficient resolution.

Here, we demonstrate a novel method that employs slow light for enhancing the optical resolution when imaging the fiber. This allows us to determine the radius profile of an optical microfiber with sub-Ångström precision while preserving high axial resolution. Slow light has attracted significant interest in recent years [15], resulting in various applications. For example, slow light emerging in photonic crystals has been utilized for realizing sensors [16–18], amplifiers [19], spatial compression of optical power densities [20, 21], and nonlinear optics [22, 23]. In this work, we make use of slow light arising in the presence of whispering gallery modes (WGMs) which naturally form around optical fibers [24]. WGMs are optical resonances, in which light travels around the circumference of the fiber, undergoing continuous total internal reflection [25]. Due to the mostly azimuthal light propagation, the effective speed of light in axial direction along the fiber is significantly reduced. In this situation, already small radius variations give rise to a strong axial potential for the light which, in turn, defines the axial mode structure of the WGM (see Fig. 1a). The slow light propagation in axial direction results in a relatively slow modulation of the spatial wavefunction of the WGM. By imaging the light tunneling from the WGM into free-space with a CCD camera, we measure the axial mode profile from which we can precisely determine the radius profile of an optical fiber over a large extent in single shot

* These authors contributed equally

† juergen.volz@tuwien.ac.at

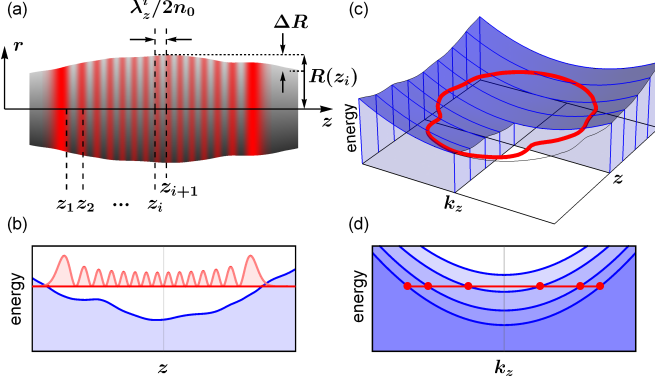


FIG. 1. (a) Side view of a fiber with nanoscale radius variation along the fiber axis. Due to these variation a characteristic mode structure forms with clear intensity maxima and minima. The distance between two adjacent intensity minima is given by the axial wavelength $\lambda_z/2n$. For the sample fiber considered here, the central radius R_0 is a few tens of micrometer and the radius variation ΔR is on the order of a few nanometer. (b) The radius profile can be translated into a potential energy $V(z)$, which can support optical bound states, i.e. localized WGMs, indicated in red. (d) Axial dispersion relation of the photon energy $\hbar\omega(k_z)$ for different fiber radii. (c) Phase space representation of a WGM with energy $\hbar\omega_q$ that is trapped in the potential formed by nanoscale radius variations along z . Projecting the plot onto the z and k_z axis yields the cases shown in (b) and (d), respectively.

operation.

II. THEORETICAL MODEL

When light circulates around the circumference of a fiber, the electric field \mathcal{E} has to fulfill the Helmholtz equation

$$(\nabla^2 + k^2 n^2(r))\mathcal{E} = 0. \quad (1)$$

Here, $k = 2\pi/\lambda$ is the length of the light's wave vector and $n(r)$ describes the refractive index in ($n = n_0$) and outside ($n \approx 1$) the fiber. When the radius variations of the fiber are sufficiently small, we can separate the propagation of the light into a propagation parallel to the fiber axis with wavevector \mathbf{k}_z and around the fiber's circumference with wavevector $\mathbf{k}_{\phi,r}$, where $\mathbf{k} = \mathbf{k}_{\phi,r} + \mathbf{k}_z$. This allows us to separate the Helmholtz equation using the Ansatz $\mathcal{E} = \Phi(\phi, r)\mathcal{Z}(z)$. For a given radius $R(z)$, the radial and azimuthal equations can locally be solved, yielding the resonance condition $k_{\phi,r}(z) = f(m, p)m/R(z)n_0$, where m and p are the azimuthal and radial quantum numbers of the WGM, respectively, and $f(m, p) \sim 1$ is a correction factor that describes the geometrical dispersion of the fiber, see supplemental material. The axial part of the system can be treated as a one-dimensional

(1D) problem, described by the axial wave equation

$$\left(\partial_z^2 + k^2 n^2 - f^2 \frac{m^2}{R(z)^2} \right) \mathcal{Z}(z) = 0, \quad (2)$$

where we made use of $k^2 = k_z^2 + k_{\phi,r}^2$. Equation (2) is formally identical to a 1D Schrödinger equation [5] and describes the propagation of a photon with effective mass $m_e = \hbar k n_0^2 / 2c$ in the potential landscape that is set by the radius profile $R(z)$ with the potential $V(z)/(2m_e/\hbar^2) = (mf)^2/R(z)^2$ (see Fig. 1b), where c is the vacuum speed of light. The local group velocity c_{gr} of light traveling along this potential can be obtained from the dispersion relation $\omega(k_z) = c/n_0 \sqrt{k_{\phi,r}^2 + k_z^2}$ (see Fig. 1d) and is approximated to be $c_{gr} = d\omega/dk_z \approx c/n_0 \cdot k_z/k$ [24]. For light fields close to the band edge $k \approx k_\phi$, one obtains a very strong reduction in group velocity, i.e. $c_{gr} \ll c$. Due to this group velocity reduction, the phase velocity of the light in axial direction $c_{ph} = c^2/(n_0^2 c_{gr})$ is strongly increased. As the axial wavelength λ_z is directly proportional to c_{ph} , λ_z is significantly larger than the vacuum wavelength. Due to this magnification effect, the axial wavelength can now be measured with high accuracy, which in turn allows one to perform a high-accuracy measurement of the axial potential of the light and, thus, of the corresponding fiber radius variations. The dependency of the local group velocity and, thus, λ_z on the fiber radius can be expressed as

$$R(z) = f \frac{m\lambda}{2\pi n_0} (1 - \mathcal{S}^2)^{-\frac{1}{2}}, \quad (3)$$

where we introduced the velocity reduction $\mathcal{S} = c_{gr}/c = \lambda/\lambda_z$. In our experiment, the axial radius variations that define the potential $V(z)$ result in bound states in axial direction. For this case, the light oscillates between the two axial turning points, called the caustics, creating a standing wave along the fiber, while still propagating along the circumference as a running wave. Measuring the intensity distribution of the axial standing wave then allows one to determine the local axial wavelength λ_z , thus, the local speed of light and the local fiber radius. Due to the slow propagation velocity in axial direction we can measure the position-dependent axial wavelength to determine the axial radius profile with enhanced precision. The enhancement factor can be expressed as

$$M = \left| \frac{\partial \lambda_z}{\partial R(z)} \right| \approx \frac{2\pi}{mf} \frac{1}{\mathcal{S}^3}. \quad (4)$$

From Eq. 4 follows that the enhancement factor and, thus, the possible resolution in radial direction, strongly increases with decreasing \mathcal{S} (increasing λ_z). The achievable radial resolution is

$$\Delta R = \frac{\Delta \lambda_z}{M}. \quad (5)$$

where $\Delta \lambda_z$ is the error in determining λ_z and is given by the optical resolution of the microscope. For typical

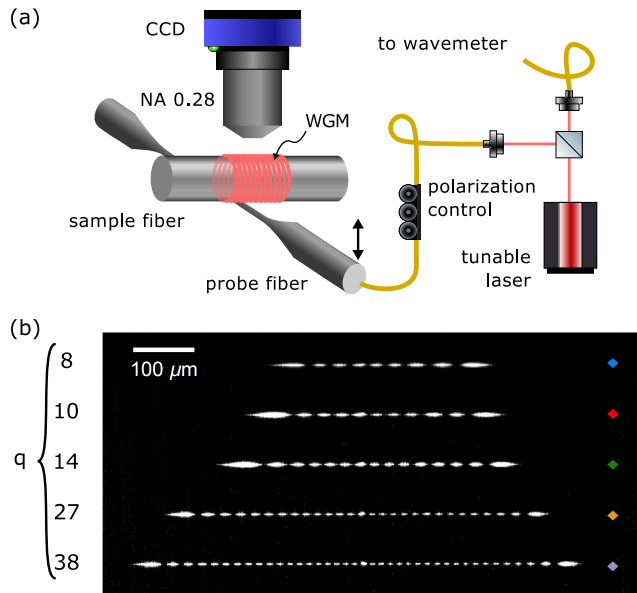


FIG. 2. (a) The experimental setup used to determine the radius profile of the sample fiber consists of a tunable diode laser, polarization controllers, a probe fiber, and a CCD camera with an $NA = 0.28$ objective. For further diagnostics, an additional photo diode can be used to monitor the fiber transmission, and the incident light is sent onto a wavelength meter. (b) Micrographs of light tunneling out of the WGMs in direction of the camera for different axial modes, $q \in \{8, 10, 14, 27, 38\}$, which are used for determining the local fiber radius in Fig. 3

experimental parameters, values of $M = 10^4 \dots 10^5$ can easily be achieved, see Table I. We note that the enhancement of the optical resolution in radial direction given in Eq. (5) is inherently connected with a decrease in axial resolution for which the resolution is approximately given by $\lambda_z/2$.

III. SETUP AND MEASUREMENT PROCEDURE

The fiber under examination is referred to as sample fiber. In order to couple light into the sample fiber, we use a tapered optical fiber with nanofiber waist. This probe fiber is mounted on a translation stage and aligned perpendicular to the sample fiber. This allows us to evanescently couple light from the probe to the sample fiber, see Fig. 2a. The coupling rate between the fibers can be adjusted via their relative distance. When light is sent through the probe fiber and its frequency is scanned, WGMs are excited whenever the radial and axial resonance condition is fulfilled and when the WGM has a finite mode overlap with the evanescent field of the probe fiber. The excited WGMs can be observed using a CCD camera that images the mode structure along the sample fiber, as shown in Fig. 2b. We emphasize that the collected light is not scattered from the surface,

but originates from tunneling of WGMs through the potential barrier imposed by the refractive index step at the fiber surface [26]. As a consequence, the imaging of the mode structure does not rely on local surface pollution or roughness, but occurs for any structure supporting WGMs. For imaging, we employed a CCD camera (mvBlueFox3, Matrix Vision) in combination with a standard microscope objective (Mitutoyo 10X M Plan APO LWD) with $NA=0.28$. The camera system is mounted on the opposite side of the probe fiber in order to have a clear view of the WGMs (see Fig. 2a). For probing the fiber, we used a tunable diode laser (Velocity Laser 6316, New Focus) with a wavelength of about 845 nm.

In order to obtain the radius profile from the camera images, such as shown in Fig. 2b, we use the following procedure. We determine the axial profile of the WGM by averaging over several horizontal pixel lines. Then the positions of zero intensity z_i are extracted from a parabolic fit to the data points in the vicinity of the intensity minima. For our imaging system, this procedure enables us to determine these positions with a precision of $\Delta\lambda_z = 0.2 \mu\text{m}$, see supplemental material. In order to obtain the absolute value of the local radius, according to Eq. (3), we also require the azimuthal and radial quantum numbers m and p of the imaged WGM. Therefore, we compare the measured azimuthal free spectral range of different mode families to the free spectral range obtained from numerically solving the radial wave equation of a dielectric cylinder, see supplemental material.

IV. RESULTS AND PRECISION

After pulling the sample fiber to approximate $30 \mu\text{m}$ diameter, we recorded two sets of images with the CCD camera. First, the probe fiber was placed approximately at the center of the sample fiber waist and we performed five independent measurements of the radius profile by exciting five TE-polarized modes with different axial quantum number q , but the same quantum numbers m and p . Figure 2b shows micrographs of the light tunneling out of the fiber for these WGMs. The resonance wavelengths measured with the wavelengthmeter as well as the corresponding q are summarized in Tab. I. The azimuthal and radial quantum numbers have been determined to be $m = 117$ and $p = 8$, which corresponds to a correction factor $f(8, 117) = 1.42605843(1)$, see supplemental material. The radius profiles of the fiber extracted from these images are shown in Fig. 3. The radius profiles obtained using different modes are in very good agreement with each other, illustrating the reproducibility of the method. It also becomes evident that with increasing axial resolution (for higher q), the radial resolution decreases, as expected for this measurement (see Eq. (5)). In order to check if the position of the probe fiber alters the measured radius profile, the measurement was repeated with the probe fiber moved by $\sim 110 \mu\text{m}$ in axial direction. The results are shown in Fig. 3b and

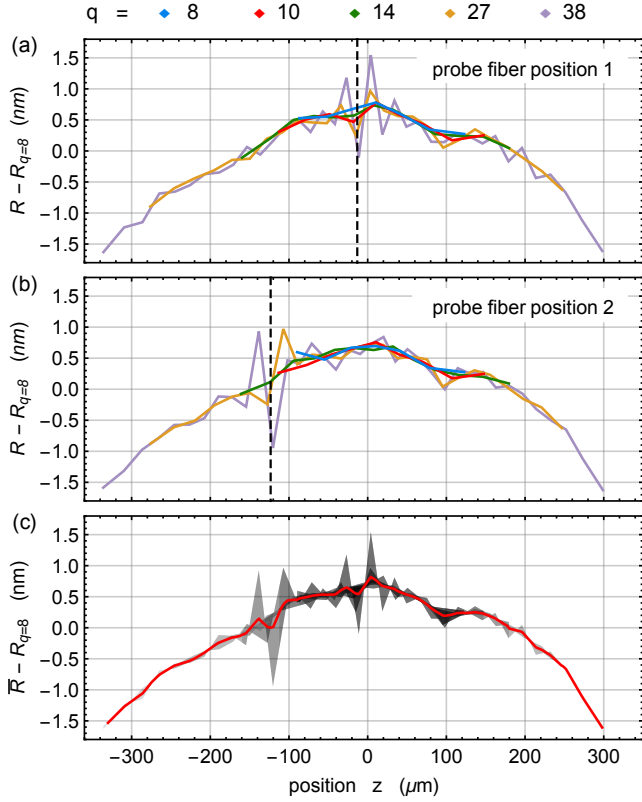


FIG. 3. (a) Evaluated radius profiles as a function of the position along the fiber for WGMs with different axial quantum number q . The position of the probe fiber is indicated by the dashed vertical line. (b) Same as (a) only with the probe fiber moved by $\sim 110 \mu\text{m}$. (c) Mean radius profile obtained when all measurements are taken into account (red line). The shaded area indicates the deviation of the individual measurements from the mean profile. For better visibility, we subtracted the caustic radius of the probe fiber for the $q = 8$ mode, $R_{q=8} = 15.475(1) \mu\text{m}$.

are in very good agreement with the measurements in Fig. 3a. In the measurements with the highest axial resolution, i.e., with the highest values of q , one observes a small distortion at the position of the probe fiber. However, the errors introduced by scattered light from the probe fiber are well below a nanometer and can be corrected by performing two measurements with different fiber positions.

Two different types of errors contribute to the measured radius profiles $R(z)$. On the one hand, there is a systematic error in the absolute radius $R_q = fm\lambda_q/n_0$ which amounts in our case to an uncertainty of around $\pm 1 \text{ nm}$. This error is identical for each measurement and originates from the systematic error in determining λ , f and n_0 in Eq. (3). For our setup, this is dominated by the limited knowledge of the refractive index of the sample fiber n_0 . Despite this, the radius variations along the fiber, $R(z) - R_q$, can be measured with much higher accuracy and are, in our measurement, limited by the

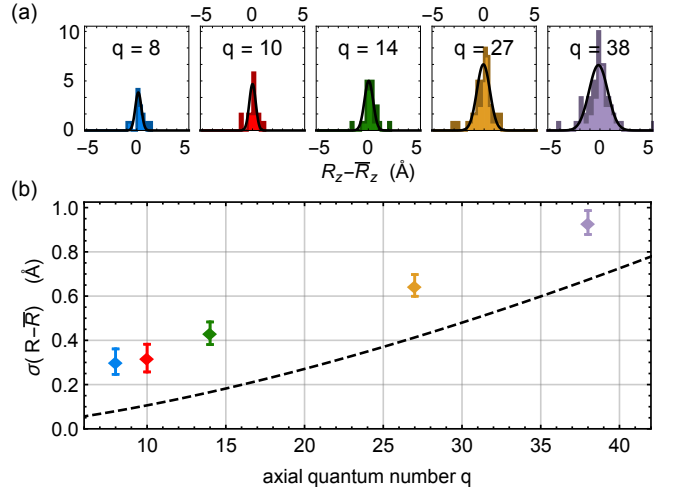


FIG. 4. (a) Histogram of the deviation for each individual measurement from the average radius profile \bar{R} for different q . (b) Standard deviation of $R - \bar{R}$, obtained from the Gaussian fits in (a), as a function of q . The error bars show the standard errors for the parameter estimates of the fit. The dashed line corresponds to the theoretically expected mean standard error calculated assuming a parabolic radius profile.

measurement accuracy of the axial wavelength λ_z , see supplemental material for more details.

TABLE I. Axial quantum number q , the resonance wavelength λ_{vac} , mean axial wavelength $\bar{\lambda}_z/n_0$, and the resulting mean enhancement factor \bar{M} of the WGMs under examination.

q	$\lambda_{vac} \text{ (nm)}$	$\bar{\lambda}_z/n_0 \text{ (}\mu\text{m)}$	\bar{S}	$\bar{M}/10^3$
8	846.4819	68.8	0.0058	190
10	846.4724	63.5	0.0063	149
14	846.4569	55.8	0.0072	101
27	846.4007	40.9	0.0098	40
38	846.3500	34.4	0.0117	24

From the in total 10 individual measurements, we determined the most likely fiber radius profile \bar{R} by linearly interpolating the measurement points for each mode and taking the average over all modes. The resulting profile is shown in Fig. 3c. It indicates an almost perfect cylinder that has a residual radius variation of 2 nm over an axial extend of $600 \mu\text{m}$. The fact that the fiber gets thinner when moving away from the center of the fiber waist is a typical artifact of the fiber pulling process.

In order to get an estimate of the precision of the individual measurements, we compute the deviation between each measurement point from the most likely radius profile, $R - \bar{R}$ and histogram the deviation for each axial mode, see Fig. 4a. The standard deviation of this difference $\sigma(R - \bar{R})$ gives an estimate of the error of our measurement of the radius variation along the fiber. Figure 4b shows this standard deviation as a function of q

and for comparison a theoretical prediction (dashed line). For calculating the theory curve, we approximate the radius profile by a parabolic profile from which we then estimate the average axial wavelength. Taking into account all known experimental errors, we derive the expected mean standard deviation of the axial radius profile, see supplementary material. Our analysis shows that the measurement precision of the radius variation increases with decreasing q , as expected. For all modes we observe sub-Ångström precision and for $q = 8$ we reach a precision of 0.30 ± 0.06 Ångström. Our precision inferred from the measurement data shows the same behaviour with q as the theoretical prediction.

V. SUMMARY AND OUTLOOK

In summary, we demonstrated a method that uses slow light to determine the radius variations along an optical fiber with sub-Ångström precision. In contrast to other fiber-probing methods, the demonstrated approach does only require approximate knowledge of the system parameters and can be performed using low cost equipment, such as a CCD camera, while still maintaining sub-

Ångström precision, see supplementary material. Furthermore, this method minimizes systematic errors and possible damage by evanescently interfacing the sample fiber. In addition, we are also able to measure the absolute value of the fiber radius, where we exceed the accuracy of most other methods.

Importantly, our results apply to any fiber or in general any optical system that supports WGMs and it can be straight forwardly be generalized to many situations where slow light occurs. Thus, our low-cost and non-destructive approach might be of use for in-situ monitoring of fiber fabrication. Finally, it could be utilized for spatially-resolved sensing [27].

ACKNOWLEDGMENTS

The authors are grateful to T. Hoinkes for technical support. This work has received funding from the European Commission under the projects ErBeStA (No. 800942) and ERC grant NanoQuaNt as well as the Austrian Science Fund under the project NanoFiRe (No. P 31115).

-
- [1] R. E. Thompson, D. R. Larson, and W. W. Webb, *Biophysical Journal* **82**, 2775 (2002).
 - [2] S. W. Hell, *Science* **316**, 1153 (2007).
 - [3] J. D. Wong-Campos, K. G. Johnson, B. Neyenhuis, J. Mizrahi, and C. Monroe, *Nature Photonics* **10**, 606 (2016).
 - [4] U. Wiedemann, K. Karapetyan, C. Dan, D. Pritzkau, W. Alt, S. Irsen, and D. Meschede, *Optics Express* **18**, 7693 (2010).
 - [5] M. Sumetsky and J. M. Fini, *Optics Express* **19**, 26470 (2011).
 - [6] J. E. Hoffman, F. K. Fatemi, G. Beadie, S. L. Rolston, and L. A. Orozco, *Optica* **2**, 416 (2015).
 - [7] Y. Semenova, V. Kavungal, Q. Wu, and G. Farrell, *Proc.SPIE* **9634**, 9634 (2015).
 - [8] J. Keloth, M. Sadgrove, R. Yalla, and K. Hakuta, *Opt. Lett.* **40**, 4122 (2015).
 - [9] L. S. Madsen, C. Baker, H. Rubinsztein-Dunlop, and W. P. Bowen, *Nano Letters* **16**, 7333 (2016), <https://doi.org/10.1021/acs.nanolett.6b02460>.
 - [10] T. A. Birks, J. C. Knight, and T. E. Dimmick, *IEEE Photonics Technology Letters* **12**, 182 (2000).
 - [11] M. Sumetsky and Y. Dulashko, *Optics Letters* **35**, 4006 (2010).
 - [12] S. Holleis, T. Hoinkes, C. Wuttke, P. Schneeweiss, and A. Rauschenbeutel, *Applied Physics Letters* **104**, 163109 (2014).
 - [13] M. van der Mark and L. Bosselaar, *Journal of Lightwave Technology* **12** (1994).
 - [14] F. Warken and H. Giessen, *Optics Letters* **29**, 1727 (2004).
 - [15] T. F. Krauss, *Nature Photonics* **2**, 448 (2008).
 - [16] Z. Shi, R. W. Boyd, D. J. Gauthier, and C. C. Dudley, *Opt. Lett.* **32**, 915 (2007).
 - [17] K. Qin, S. Hu, S. T. Retterer, I. I. Kravchenko, and S. M. Weiss, *Opt. Lett.* **41**, 753 (2016).
 - [18] C. Kraeh, J. Martinez-Hurtado, A. Popescu, H. Hedler, and J. J. Finley, *Optical Materials* **76**, 106 (2018).
 - [19] S. Ek, P. Lunnemann, Y. Chen, E. Semenova, K. Yvind, and J. Mork, *Nature Communications* **5**, 5039 (2014).
 - [20] J. F. McMillan, X. Yang, N. C. Panoiu, R. M. Osgood, and C. W. Wong, *Opt. Lett.* **31**, 1235 (2006).
 - [21] S. Yan, X. Zhu, L. H. Frandsen, S. Xiao, N. A. Mortensen, J. Dong, and Y. Ding, *Nature Communications* **8**, 14411 (2017).
 - [22] B. Corcoran, C. Monat, C. Grillet, D. J. Moss, B. J. Eggleton, T. P. White, L. O'Faolain, and T. F. Krauss, *Nature Photonics* **3**, 206 (2009).
 - [23] C. Xiong, C. Monat, A. S. Clark, C. Grillet, G. D. Marshall, M. J. Steel, J. Li, L. O'Faolain, T. F. Krauss, J. G. Rarity, and B. J. Eggleton, *Opt. Lett.* **36**, 3413 (2011).
 - [24] M. Sumetsky, *Phys. Rev. Lett.* **111**, 163901 (2013).
 - [25] Matsko and V. Ilchenko, *IEEE Journal of Selected Topics in Quantum Electronics* **12**, 3 (2006).
 - [26] M. Tomes, K. J. Vahala, and T. Carmon, *Optics Express* **17**, 19160 (2009).
 - [27] M. Foreman, J. Swaim, and F. Vollmer, *Advances in Optics and Photonics* **7**, 168 (2015).

Supplemental material

I. GEOMETRIC DISPERSION

The dispersion of light in WGMs depends not only on the resonator's material but also on its geometry. This stems from the fact that the radial distribution, inside and outside of the resonator material, for a given wavelength, is strongly related to the resonator's geometry. As a consequence, when changing the resonators dimensions the resonance spectrum also changes. In the following the geometric dispersion will be treated by solving the radial wave equation.

By making use of the cylindrical symmetry and separating the Helmholtz equation Eq. (1), the radial differential equation, after solving the azimuthal part, is

$$\partial_r^2 \Phi(r) + \frac{1}{r} \partial_r \Phi(r) + \left(k_{\phi,r}^2 - \frac{m^2}{r^2} \right) \Phi(r) = 0. \quad (\text{S1})$$

Here, (r, ϕ, z) are the cylindrical coordinates, $\Phi(r)$ is the radial wave function, m the azimuthal quantum number, and $k_{\phi,r}$ the component of the wave vector in the (ϕ, r) -plane. The solutions are given by the Bessel function of the first kind, J_m , and the Bessel function of the second kind, Y_m . Resonances of a cylindrical resonator with radius R can then be found by solving a transcendental equation, that implements the boundary conditions imposed by Maxwell's equations. The transcendental equation reads

$$P \frac{J'_m(knR)}{J_m(knR)} = \frac{Y'_m(kR)}{Y_m(kR)}, \quad (\text{S2})$$

where $P = n_0$ or $1/n_0$ for TE and TM modes, respectively [1]. An exact analytic solution of Eq. (S2) is generally not possible, such that resonance frequencies must be determined either numerically or by means of analytical approximations. The resulting component of the wave vector can be expressed as

$$k_{\phi,r}(z) = f(m, p) \frac{m}{n_0 R(z)}, \quad (\text{S3})$$

where $f(m, p)$ accounts for the geometric dispersion, and the radial quantum number, p , indicates the p th root of Eq. (S2). In order to illustrate the dependencies of $f(m, p)$, it can be approximated by, e.g., the asymptotic expansion [2]

$$f(m, p) \approx 1 + \frac{\alpha_p}{2^{1/3} m^{2/3}} - \frac{P}{m(n_0^2 - 1)^{1/2}} + \frac{3}{10} \frac{\alpha_p^2}{2^{2/3} m^{4/3}} - \frac{P(n_0^2 - 2P/3)}{(n_0^2 - 1)^{3/2}} \frac{\alpha_p}{2^{1/3} m^{5/3}} + \dots, \quad (\text{S4})$$

where α_p are the p th root of the Airy function [3]. In Figure 1, the geometric dispersion factor $f(m, p)$ is plotted for different quantum numbers m and p .

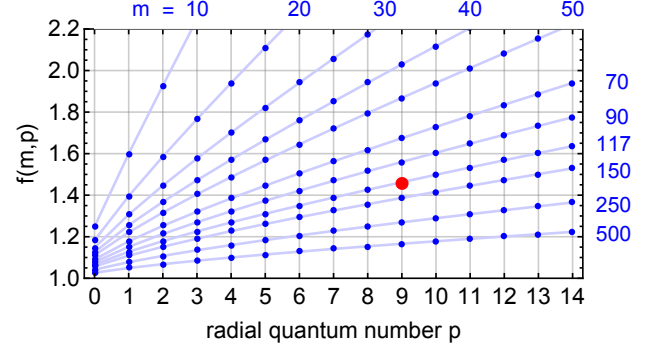


FIG. 1. Geometric dispersion factor $f(m, p)$ for different azimuthal quantum numbers m as a function of the radial quantum number p and $n_0 = 1.4526$. The red dot indicates the value for the modes used in this manuscript.

II. DETERMINATION OF THE RADIAL AND AZIMUTHAL QUANTUM NUMBER

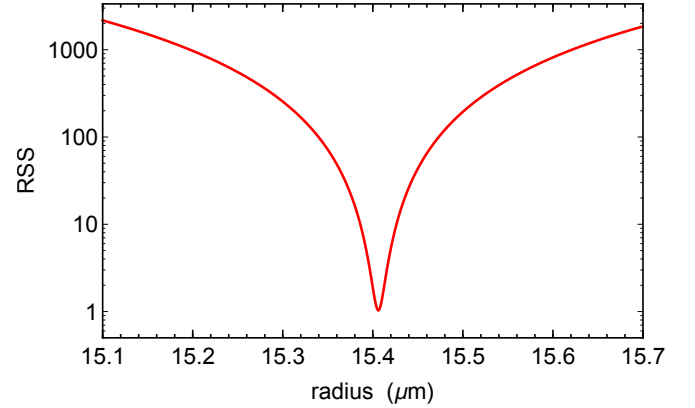


FIG. 2. Minimal residual sum of squares (RSS) of the measured and calculated azimuthal free spectral ranges as a function of the fiber radius R for the optimal set of m and p .

In order to determine the exact axial quantum numbers m and p of the analyzed WGM, we compared the azimuthal free spectral range (azFSR) measured in the experiment to the azFSR calculated using the numerical solution of Eq. (S2). In particular, we measured the azFSR of the fundamental axial mode for three different mode families. The calculated azFSR has two discrete and one continuous free parameters, m , p and the radius R . Thus, we try to find the best estimate for R by calculating the azFSRs for a large set of quantum numbers m and p , and compute the residual sum of squares (RSS) to the measured azFSRs. The minimal RSS for the set of parameters given in Tab. I as a function of the radius

R is shown in Fig. 2. Mode pair # 1 belongs to the same mode family as the modes used in the manuscript, thus yielding the quantum numbers m and p .

TABLE I. Set of quantum numbers used to obtain a minimal RSS of the measured and calculated azFSRs

mode pair #	m	$m+1$	p
1	117	118	8
2	121	122	7
3	134	135	4

III. ESTIMATION OF THE MEASUREMENT ERROR

In order to derive an expression for the error in the estimation of the axial radius variations, studied in the main manuscript, we start with Eq. (3), which can be approximated, for the case of $\lambda \ll \lambda_z$, by

$$R(z) = R_q + \frac{R_q}{2} \left(\frac{\lambda_q n_0}{\lambda_z(z)} \right)^2, \quad (S5)$$

where $R_q = f(m, p)m\lambda_q/2\pi n_0$ is the radius at the caustic of the axial mode with quantum number q and vacuum wavelength λ_q . The refractive index of the resonator material, n_0 , enters here because the axial wavelength measured via the imaging corresponds to λ_z/n_0 . In this form, one can separate the error of the local radius $R(z)$ into an error of the absolute caustic radius R_q and an error for the axial variations around R_q given by the second term in Eq. (S5). The relative error of R_q is given by

$$\begin{aligned} \frac{\Delta R_q}{R_q} = & \left(\frac{\partial f}{\partial m} + \frac{1}{m} \right) \Delta m + \frac{\partial f}{\partial p} \Delta p \\ & + \left(\frac{\partial f}{\partial n_0} + \frac{1}{n_0} \right) \Delta n_0 + \frac{\Delta \lambda_q}{\lambda_q} \end{aligned} \quad (S6)$$

and the error for the radius variations $R - R_q$ is given by

$$\frac{\Delta(R - R_q)}{R - R_q} = \left(1 + \frac{\Delta R_q}{R_q} + 2 \frac{\Delta n_0}{n_0} + 2 \frac{\Delta \lambda_q}{\lambda_q} \right) \cdot 2 \frac{\Delta \lambda_z}{\lambda_z} \quad (S7)$$

where the errors on R_q , λ_q and n_0 only enter as a global factor into the error of the radius variation, as these quantities are constant for the whole measurement. As a consequence, the error for the radius profile is in most relevant cases dominated by the error in the measurement of λ_z .

Table II shows the uncertainties of the different quantities for our experiment and their contribution to the error in measuring the caustic radius R_q and the axial radius variations. In more detail, the light's wavelength λ_q was measured using a wavemeter (High Finesse WS7-60) with a specified absolute accuracy

TABLE II. Error budget of the absolute radius σ_R and the radius variation σ_{R-R_q} , for $\lambda'_z = 50 \mu\text{m}$

Error source	error	σ_{R_q} (pm)	σ_{R-R_q} (pm)
n_0	10^{-5}	106	10^{-3}
λ	1.4×10^{-5} nm	0.3	10^{-6}
λ_z	$0.2 \mu\text{m}$	8.4	0.5
f	$< 10^{-7}$		

of 60 MHz which for our wavelength corresponds to $\Delta\lambda_q = 1.4 \times 10^{-5}$ nm. The discrete quantum numbers m and q are directly obtained from our fitting procedure and, thus, do not contribute to the error. Another error source originates from the not precisely known refractive index n_0 which we obtained from the Sellmeier equations given in Ref. [4]. As an estimate for the error of the refractive index of our fiber we use the maximal residuals in Ref. [4], that amounts to $\Delta n_0 = 10^{-5}$ at 850 nm wavelength. Compared to this, the error of n_0 due to the wavelength error can be neglected. The geometric dispersion also depends on the refractive index of the fiber and the surrounding material. Using the approximation by Lam [2] this can be estimated to be $|df/dn_0| < 0.01$ for a large range of quantum numbers m and p . Including the refractive index of air instead of vacuum changes f by 10^{-7} . To determine the axial wavelength λ_z , we locally fitted a parabolic curve to the axial intensity profile. To estimate the error of this fitting procedure, Poisson noise according to our experimental signal to noise level was added to the measured data and then fitted again. The standard deviation of the resulting minimum positions then yields an uncertainty in the axial wavelength determination of $\Delta\lambda_z = 0.2 \mu\text{m}$. Consequently, in our experiment, the uncertainty in R_q is dominated by the uncertainty of the refractive index n_0 , while for the radius variation the dominant error source are the measurement errors of the axial wavelength, λ_z , when imaging the wavefunctions.

As mentioned in the main manuscript, the optical measurement of the radius profile is very robust even if the the exact experimental parameters are not known. To illustrate this, we also consider the case, where one does not have access to a wavemeter, so the resonance wavelength can not be determined precisely. In this case, the individual errors are significantly larger. For this, we assume the errors $\Delta n_0 = 0.01$ and $\Delta\lambda_q = 1$ nm which can, e.g., be obtained by using a simple grating spectrometer. In this case, the determination of the radial and azimuthal quantum numbers p and m will not work which would result in an increased uncertainty on these parameters and consequently on the geometric dispersion factor $f(m, p)$. However, one can directly obtain an estimate of the absolute radius of the fiber R_q using standard microscopy. If we assume an error of about $\Delta R_q = 0.5 \mu\text{m}$ for a fiber radius of $15 \mu\text{m}$ as in our experiment, the obtainable precision in the radius variations $R - R_q$ based

on our slow-light imaging method is not significantly reduced, as the first factor in Eq. (S7) is still approximately equal to one. Remarkably, even in this case, one retains sub-Ångström precision.

IV. MEAN STANDARD DEVIATION FOR A PARABOLIC RADIUS PROFILE

In order to estimate the scaling of the mean standard error as a function of the axial quantum number q that is plotted in Fig. 4b, we assume a parabolic radius profile

$$R(z) = R_0 \left(1 - \frac{(\Delta k z)^2}{2} \right). \quad (\text{S8})$$

Here, R_0 is the central radius and Δk the curvature of the profile, which was obtained from a fit to the experimental data $\Delta k = 0.000052 \mu\text{m}^{-1}$. In order to get the mean spacing between two intensity minima, we assume that the mode extends between the classical turning points, i.e., the two caustics and divide it by the number of intensity maxima, $q + 1$. The resulting mean axial wavelength $\overline{\lambda_z}$ can be inserted into Eq. (5) to obtain the theoretically expected mean standard deviation shown in Fig. 4b.

-
- [1] A. Oraevsky, Quantum Electronics **32**, 377 (2002).
 [2] C. C. Lam, P. T. Leung, and K. Young, Journal of the Optical Society of America B **9**, 1585 (1992).

- [3] M. Abramowitz, I. A. Stegun, and D. Miller, *Handbook of Mathematical Functions With Formulas, Graphs and Mathematical Tables*, 10th ed. (Dover Publications, 1964).
 [4] I. H. Malitson, Journal of the Optical Society of America **55**, 1205 (1965).